

# Meshless Helmholtz-Hodge Decomposition of Glacier Velocities.

Matthew Walloch

December 2, 2025

## Abstract

Hodge decomposition is a technique in which we can visualize vector fields on Riemannian manifolds by decomposing them into three orthogonal components: a divergence-free, curl-free, and harmonic part. Our main question is can we apply this technique to glacier velocity fields to better visualize ice flow? We will use simulated flow fields to get a nice continuous dataset, although there are ways to extend a discrete points into a continuous vector field. Based on other studies using this technique, we anticipate the harmonic component will be analogous to the general flow of the glacier. The divergence-free should display if there is any swirling or circular flow. The curl-free might display where there is accumulation or oblation but this is a guess. The main challenge we anticipate is the size of the dataset and the time complexity. Another struggle will be how to display the results in a way that sense on a flat page.

## Introduction

Our goal is to decompose vector fields of ice velocities. In order to do this we have to first define how we can think of the glacier mathematically. In this paper, a manifold will be a smooth topological manifold with boundary, that being a space  $X \subset \mathbb{R}^n$  such that for all  $x \in X$ , a small enough neighborhood of  $x$ ,  $U(x)$ , "looks like" a lower-dimensional Euclidean space. Mathematically, we denote this  $U(x) \cong \mathbb{R}^m$  or  $U(x) \cong \mathbb{R}_+^m$  for all  $x \in X$  with  $m < n$ . At each point in the manifold, we can give it a vector, i.e.,  $T_p : M \rightarrow \mathbb{R}^n$ . This essentially turns our manifold into a Riemannian manifold. In any case, a glacier equipped with velocities at each point will meet this definition.

We will begin with an overview of Helmholtz-Hodge decomposition. We can start with the most general Hodge decomposition, for this we can use a modification of [4].

**Theorem 1.1** (Hodge Decomposition with Boundary (Hodge-Morrey)). *Let  $M$  be a compact, orientated, Riemannian manifold with boundary  $\partial M$ . Let  $\Omega^k(M)$  be the space of smooth weakly differentiable  $k$ -forms,  $\vec{d}$  be the exterior derivatives on  $\Omega^k$ , and  $\vec{\delta}$  be the codifferential operator, then we can decompose  $\Omega^k$ , into*

$$\Omega^k = \vec{d}\Omega_t^{k-1} \oplus \vec{\delta}_n^{k+1} \oplus H^k$$

with

$$\Omega_t^{k-1}(M) = \{\alpha \in \Omega^{k-1}(M) \mid \alpha \text{ parallel to } \partial M\}$$

$$\Omega_n^{k+1}(M) = \{\alpha \in \Omega^{k+1}(M) \mid \alpha \text{ normal to } \partial M\}$$

$$H^k(M) = \{\alpha \in \Omega^k(M) \mid \alpha \text{ harmonic}\}$$

with parallel and normal being with respect to the metric on  $M$ .

The proof of this relies on de-Rham cohomology which is beyond the scope of this paper. This theorem lays the groundwork for what we can do; however is a bit far removed in practice. In  $\mathbb{R}^3$  we can be a little more specific in our decomposition; in this case, we get the following formulation via [1].

**Theorem 1.2** (Helmholtz-Hodge Decomposition in  $\mathbb{R}^3$ ). *Let  $V$  be a smooth vector field on a closed, bounded manifold  $M$  with boundary  $\partial M$ . Then we can decompose  $V$  into a gradient-free, divergence-free, and harmonic component as*

$$V = \nabla u + \nabla \times w + h$$

with  $u$  a scalar potential and  $w$  being a vector potential function.

It is important to note that there are a few variations of this decomposition, from 2 to 5 component decompositions. The gradient-free and divergence-free remain relatively similar in every case, with the harmonic component usually being split up in order to capture more topological aspects of the manifold.

This theorem is the general motivation of Helmholtz-Hodge algorithms. However, in practice, the algorithms are in a discrete setting, either using a triangulated mesh or point cloud to calculate an approximation of the vector field decomposition. In our specific case, we will use a point cloud approximation as that is what our data is already in [2].

As for the applications of Helmholtz-Hodge or Helmholtz-Hodge like decompositions, they are often used in fluid dynamics, either to satisfy requirements of certain solutions or to visualize flows [2]. It has also been used in oceanography to help visualize flows and detect eddies [6]. A more abstract version has been used to RNA-velocities to visualize the cell differentiation [5], in which they projected thousands of dimensions of data into  $\mathbb{R}^2$  and then decomposed that. Thus, there are many ways to apply Helmholtz-Hodge decomposition in terms of visualization and identification processes. So we will investigate an application of Helmholtz-Hodge decomposition to glacier velocities, which, to our knowledge, has not been done before.

In terms of the specifics of the glacier, we are using data from [3], which used a full-Stokes approximation of two regions in the Northeast Greenland Ice Stream, one being an ice stream and one being an outlet. Both have slow and fast-moving ice and variable bed topography, so we hope that this will lead to interesting visualizations in the decomposed vector fields.

## Methods

### 2.1 Glacier Data

The data we retrieved from [3] is in the form of points from the top and bottom of the glacier and the velocities at each point at a variety of resolutions. The ice stream and outlet are from the 79° North Glacier and Zacharias Isbræ. They used both full-Stokes and a Blatter-Pattyn formulation. For this paper, we focused on the full-Stokes data. They used both a  $P2 + P1$  Lagrange elements, that being a quadratic basis for velocity and linear for pressure and  $P1 + P1$  Lagrange elements being linear in both. For the boundary condition, they used two different implementations for the Dirichlet condition on the base. One being a strong implementation that applies the constraints at each node in a point-wise manner. The other being a weak implementation using exterior facing integrals via the Lagrange multiplier method. They also used differing enhancement factors,  $E$ , and for this exploration, we are choosing values of 1 and 6. They also included differing sliding exponents,  $m$ , with value of 1 or 3.

### 2.2 Discrete, meshless Helmholtz-Hodge Decomposition

As the setup, we start with some vector field  $v : P \rightarrow \mathbb{R}^3$  over a set of points  $P = \{p_i\}_{i=1}^t$ . Then, we choose a group of centers,  $C = \{c_i\}_{i=1}^k$ , and a kernal  $\phi : \mathbb{R} \rightarrow \mathbb{R}$  defined as

$$\phi_i(p) = \phi(\|c_i - p\|_2) = e^{-\sigma \|c_i - p\|_2^2}$$

There are many choices for centers, including the parameter  $\sigma$ . In the context of our trials, we used  $\sigma = 1e-5$ .

Then we will describe how computation process for each component.

#### 2.2.1 Gradient-free field: $\nabla u$

Let

$$\varphi_i(p) = \nabla \phi_i(p) = \phi'_i(p) \frac{p - c_i}{\|p - c_i\|_2}$$

Then we can define a least squares system  $\Phi\alpha = \tilde{v}$  with

$$\Phi = \begin{bmatrix} \Phi_1 \\ \Phi_2 \\ \Phi_3 \end{bmatrix} \in \mathbb{R}^{3t \times k}, \quad \tilde{v} = \begin{bmatrix} v_x \\ v_y \\ v_z \end{bmatrix} \in \mathbb{R}^{3t}$$

$$\Phi_i = \begin{bmatrix} (\varphi_1(p_1))_i & (\varphi_2(p_1))_i & \dots & (\varphi_k(p_1))_i \\ (\varphi_1(p_2))_i & (\varphi_2(p_2))_i & \dots & (\varphi_k(p_2))_i \\ \vdots & \vdots & \ddots & \vdots \\ (\varphi_1(p_t))_i & (\varphi_2(p_t))_i & \dots & (\varphi_k(p_t))_i \end{bmatrix} \in \mathbb{R}^{t \times k}$$

with  $(\varphi_1(p_1))_i$  being the  $i$ th component of  $\varphi_1$ . Then, for the sake of computational simplicity, we can solve the least squares system  $\Phi^T \Phi \alpha = \Phi^T \tilde{v}$  for  $\alpha$ . Then the gradient-free field will be

$$\nabla u(p) = \sum_{i=1}^k \alpha_i \varphi_i(p).$$

### 2.2.2 Divergence-free field: $\nabla \times w$

First, we compute the block matrix

$$A = \left[ \begin{array}{c|c|c} 0 & -\partial_z \phi & \partial_y \phi \\ \hline \partial_z \phi & 0 & -\partial_x \phi \\ \hline -\partial_y \phi & \partial_x \phi & 0 \end{array} \right] = \left[ \begin{array}{c|c|c} 0 & -\Phi_3 & \Phi_2 \\ \hline \Phi_3 & 0 & -\Phi_1 \\ \hline -\Phi_2 & \Phi_1 & 0 \end{array} \right] \in \mathbb{R}^{3t \times 3k}$$

with  $\Phi_i$  being the same as defined in the previous section and each entry of the matrix being in  $\mathbb{R}^{t \times k}$ . Then we solve the least squares system  $A^T A \alpha = A^T \tilde{v}$ , again with  $\tilde{v}$  being defined in the previous section. Let

$$\alpha = \begin{bmatrix} \alpha^{(1)} \\ \alpha^{(2)} \\ \alpha^{(3)} \end{bmatrix}.$$

Then we can define the divergence-free is

$$\nabla \wedge w(p) = \left( \sum_{i=1}^k \alpha_i^{(3)} (\varphi_i(p))_2 - \alpha_i^{(2)} (\varphi_i(p))_3, \sum_{i=1}^k \alpha_i^{(1)} (\varphi_i(p))_3 - \alpha_i^{(3)} (\varphi_i(p))_1, \sum_{i=1}^k \alpha_i^{(2)} (\varphi_i(p))_1 - \alpha_i^{(1)} (\varphi_i(p))_2 \right).$$

### 2.2.3 Harmonic field: $h$

To compute the harmonic component, we can just do

$$h(p) = v(p) - \nabla u(p) - \nabla \times w(p).$$

## 2.3 Implementation details

The least squares solutions will be unique as the kernel is positive definite. To compute the centers, we used scipy's BisectingKMeans to compute around 2000 centers, but in practice, we would use as many as possible. We also used a resolution of 1600m, better resolutions would increase the cost beyond what was available. We also replaced the sums with vector and matrix operations for computation time, but left them as sums here for readability. The plotting was done in Paraview.

# Results

## 3.1 Outlet Glacier

Table 1 and Table 2 display the Helmholtz-Hodge decomposition of the outlet glacier for differing scenarios. In this case, Table 1 has a strong boundary condition, has  $E = 1$ ,  $M = 1$ , and is in the  $P_1 + P1$  regime. Table 2 again has a strong boundary condition, has  $E = 1$ ,  $M = 3$ , and is in the  $P_2 + P1$  regime. Even though we have differing regimes, we see that the decompositions are still very similar. We notice an interesting condition for the gradient-free and divergence-free that has the largest magnitude in the middle. This could be due to the calculation process, where the more central ones are more affected by the kernel. The harmonic

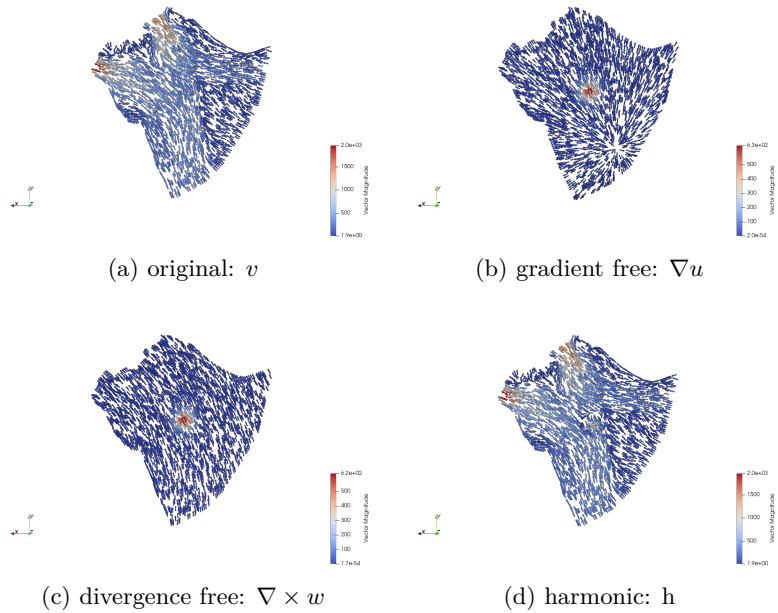


Table 1: The outlet glacier with parameters  $E = 1$  and  $M = 1$  in the  $P1 + P1$  regime

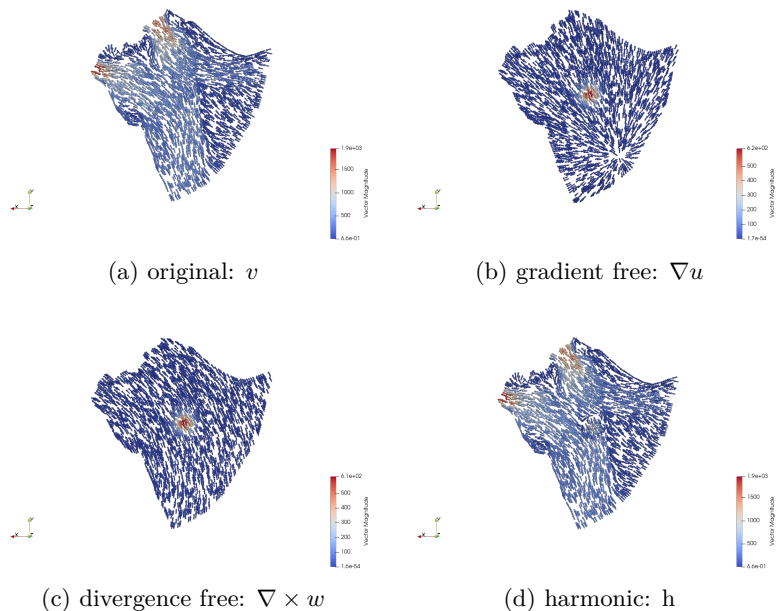


Table 2: The outlet glacier with parameters  $E = 1$  and  $M = 3$  in the  $P2 + P1$  regime

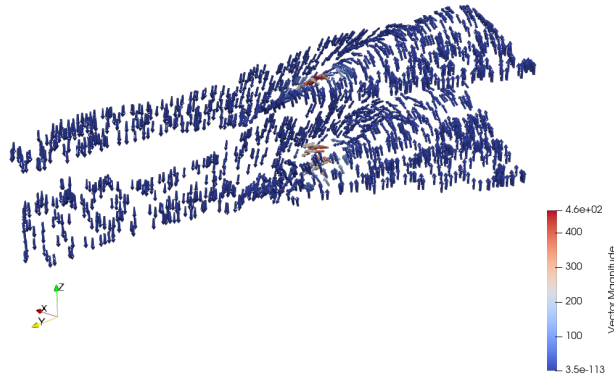


Figure 1: Side view of the divergence free field,  $\nabla \times w$ , in Table 4

one is the interesting part. We can see that it captures the flow, including the higher velocity areas very well. One thing of note is the middle, where the gradient free and divergence free are largest, the harmonic is smallest, and displays a semi-swirl behavior. This could be the saddle point of the flow, where one side does not cross over to the other.

### 3.2 Ice Stream Glacier

For the ice stream, we can see that the main difference between Table 3 and Table 4 is the enhancement factor, which, in this case, increased the magnitudes of the vectors and also caused more random patterns. For Table 3, we can see there is very little divergence and the gradient free field is relatively straightforward, again with the highest magnitudes in the middle. The divergence-free field displays an interesting swirl pattern, with the highest magnitude again being in the middle of the glacier. This could be due to the geometric properties of the glacier that force the flow in a swirling manner globally. The middle of the swirl might be the point where the corner is starting to affect the upstream behavior. The harmonic field again displays the general flow, and the point of highest magnitude in the middle seems to display the start of the flow, where it is moving the thinner downstream section.

Table 4 displays a similar story, albeit with higher magnitudes. The gradient-free is interesting as there seems to be negative divergence at the thinnest point of the stream. The harmonic seems to be similar to Table 3, although it seems the larger enhancement factor has caused there to be a lot more noise in the direction of the vectors.

The harmonic part of Table 4 is interesting, as the rest of the fields display relatively low z components. However, the side view of the divergent free reveals that the upstream glacier has a large positive z component, while the negative y side and downstream portions display a large negative z component. This could be due to the overall flow of the glacier downwards, while the positive z could be from the interactions with the bed topography. The reason this is mitigated in Table 3 could be the lower enhancement factor.

## Discussion

Overall, there seems to be a pattern of behavior in the decomposed fields. We see that in the divergence-free and gradient-free, free have a region in the center in the highest magnitudes. We conjecture this is due to the centers having the most influence in the centroid of the glacier. This could be lessened, or disappear with a different kernel choice or change in parameter  $\sigma$ . We see the gradient-free display either a single point of divergence or a single flow. this makes sense as ice is essentially incompressible. However, the times there is an interesting behavior, it seems to show ice either diverting from a large area, like in Tables 1 and 2, or diverging into a narrow area, like in Table 3.

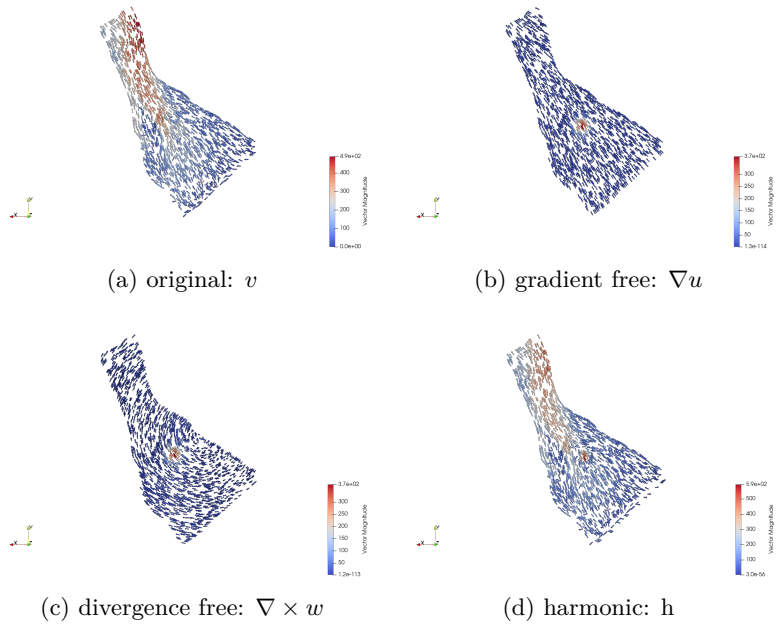


Table 3: The icestream glacier with parameters  $E = 1$  and  $M = 1$  in the  $P1 + P1$  regime

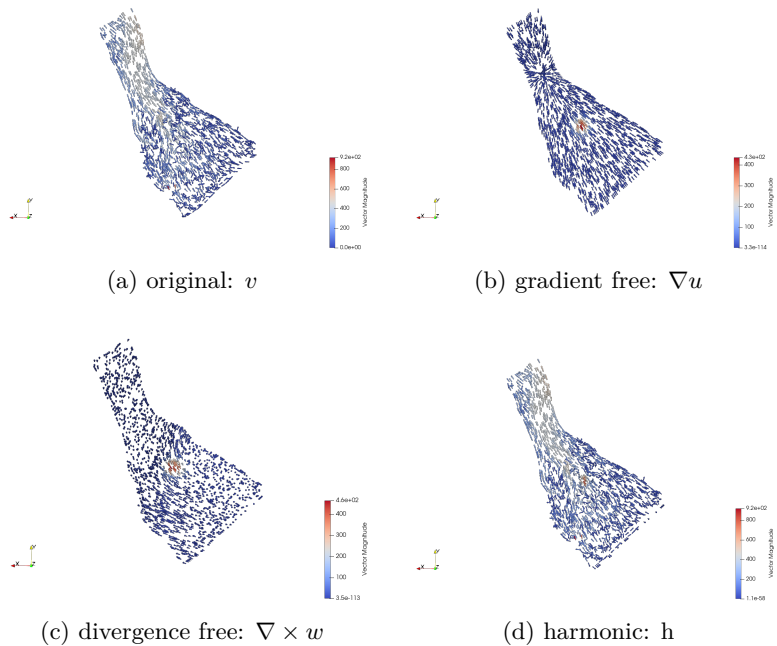


Table 4: The icestream glacier with parameters  $E = 6$  and  $M = 1$  in the  $P1 + P1$  regime

The divergence-free field again has a center region with the largest magnitude and looks to display the overall global flow of the glacier in the context of its geometry. In Tables 1 and 2, it curves in a clockwise manner, as that is how the glacier's geometry seems to be forcing the ice to flow. In Tables 3 and 4, we see it curves in a clockwise manner, again due to the geometry of the glacier and how it forces the ice to flow. However, in Table 4, we see that the harmonic has a large z component, which might be due to the larger enhancement factor in the simulations.

The harmonic component seems to tell the most. It is relatively similar to the overall field but seems to better display the flows and points of convergence or divergence of these flows. The harmonic component in Table 4 seems to deviate slightly from that, which is probably due to the higher enhancement factor.

Overall, this technique seems to show some information about the glacier and how ice is flowing in the glacier. One future direction we could take is to check more glaciers and see how those compare with what we have now. Another one would be to see if any of the properties of the decomposed fields correlate with other properties of the glacier. By this, we mean the magnitude of the divergence-free field might be related to the pressure or some stress on the ice. However, this would be mostly guesswork, and a much larger pattern of matching would have to be established before we would feel comfortable in prescribing this as a method to observe behavior.

One aspect that might make the Helmholtz-Hodge decomposition less useful for glaciers is that there is not as much turbulence as you would see in less viscous liquid or gas; as a result, there would be less information to visualize about the original vector field. Another direction for the application of Helmholtz-Hodge to glaciers would be to use a meshed version of the discrete decomposition. This would require a lot more data and computational power than where not available to us at this moment. This would, however, reveal better resolution and perhaps a more accurate representation of the decomposition, although, in any discrete setting, there will be some error regardless.

## Data and Code

The code for this project is available at <https://github.com/MatthewWaloch/Meshless-Helmholtz-Hodge-Decomposition-of-Glacier-Velocities>. The dataset used is available at <https://zenodo.org/records/6406103>.

## References

- [1] Harsh Bhatia et al. “The Helmholtz-Hodge Decomposition—A Survey”. In: *IEEE Transactions on Visualization and Computer Graphics* 19.8 (2013), pp. 1386–1404. DOI: [10.1109/TVCG.2012.316](https://doi.org/10.1109/TVCG.2012.316).
- [2] Faniry H. Razafindrazaka et al. “A Consistent Discrete 3D Hodge-type Decomposition: implementation and practical evaluation”. In: *ArXiv* abs/1911.12173 (2019). URL: <https://api.semanticscholar.org/CorpusID:208310119>.
- [3] M. Rückamp, T. Kleiner, and A. Humbert. “Comparison of ice dynamics using full-Stokes and Blatter-Pattyn approximation: application to the Northeast Greenland Ice Stream”. In: *The Cryosphere* 16.5 (2022), pp. 1675–1696. DOI: [10.5194/tc-16-1675-2022](https://doi.org/10.5194/tc-16-1675-2022). URL: <https://tc.copernicus.org/articles/16/1675/2022/>.
- [4] Günter Schwarz. *Hodge decomposition - a method for solving boundary value problems*. Springer Berlin / Heidelberg, 2006.
- [5] Zhe Su, Yiying Tong, and Guo-Wei Wei. “Hodge Decomposition of Single-Cell RNA Velocity”. In: *Journal of Chemical Information and Modeling* 64.8 (Apr. 2024), pp. 3558–3568. ISSN: 1549-9596. DOI: [10.1021/acs.jcim.4c00132](https://doi.org/10.1021/acs.jcim.4c00132). URL: <https://doi.org/10.1021/acs.jcim.4c00132>.
- [6] Cuicui Zhang et al. “Helmholtz–Hodge decomposition-based 2D and 3D ocean surface current visualization for mesoscale eddy detection”. In: *Journal of Visualization* 22.2 (Apr. 2019), pp. 231–243. ISSN: 1875-8975. DOI: [10.1007/s12650-018-0534-y](https://doi.org/10.1007/s12650-018-0534-y). URL: <https://doi.org/10.1007/s12650-018-0534-y>.